processes

MDPI

Article

Calcined Coal Gangue Fines as the Substitute for Slag in the Production of Alkali-Activated Cements and Its Mechanism

Chenxu Liu, Changbai Wang *, Jianyang Wu and Mengcheng Gao

School of Civil Engineering and Architecture, Anhui University of Science and Technology, Huainan 232001, China
* Correspondence: chbwang@126.com

Abstract: Nowadays, upcycling coal gangue into aggregates has become a popular method; nevertheless, the utilization of coal gangue fines (CGFs), a secondary waste generated during the production of coal gangue aggregates, is rarely concerned. This paper attempted to upcycle calcined CGFs at 800 °C as the partial substitution of slag to prepare alkali-activated cement (AAC). The variation in macroscopic compressive strength of AAC was studied, and the hydration mechanism of AAC was explored in depth by microstructure. AAC with CGFs shows tremendous advantages in compressive strength and hydration products. In the 10% calcined CGF content, the 3 d, 7 d, and 28 d compressive strengths of AAC displayed pronounced increases of 8%, 25%, and 13%, respectively. The study results showed that CGFs could replace the small amount of slag in AAC while providing a new theoretical guide and technical support for upcycling CGF into helpful material.

Keywords: coal gangue fines (CGFs); alkali-activated cement (AAC); compressive strength; microstructure; hydration products

Citation: Liu, C.; Wang, C.; Wu, J.; Gao, M. Calcined Coal Gangue Fines as the Substitute for Slag in the Production of Alkali-Activated Cements and Its Mechanism. *Processes* **2022**, *10*, 1557. https://doi.org/10.3390/pr10081557

Academic Editors: Yibing Zuo, Guang Ye and Xiaomei Wan

Received: 16 July 2022
Accepted: 5 August 2022
Published: 8 August 2022

1. Introduction

Coal gangue (CG) is the solid waste produced during coal mining and processing, accounting for approximately 10–25% of the total coal production [1–3]. As a result of the total stockpile of CG exceeding 7 billion tons in China [4], the long-term accumulation of large amounts of CG pollute water and air and occupies land resources [5]. Because CG has a chemical composition similar to clay minerals, it can be used as a building material [6–8]. The standard CG disposal method now uses CG as a coarse aggregate or fine aggregate of concrete. For instance, Salguero et al. [9] replaced part of the fine aggregate with CG, revealing the fitness of the new material for macroscopic strength, reaching higher macroscopic mechanical properties than traditional concrete. Li et al. [10] found that CG replaces natural gravel as an aggregate and analyzed the micromechanical properties of concrete by adjusting different water–cement ratios to explore the feasibility of CG replacing natural gravel entirely. Zhou et al. [11] studied the influence of the type and content of CG aggregate on the macroscopic properties of concrete. The results showed that the macroscopic mechanical properties of CG coarse aggregate concrete could meet the design requirements of C30 concrete, and it is suitable for the configuration of medium- and low-strength concrete. In addition, CG as precursors to prepare/produce alkali-activated cement (AAC) can replace Portland cement. Secondly, CG as a coarse/fine aggregate can replace natural gravel, which has significant economic and ecological benefits. Han et al. [12] investigated the preparation of AAC with water glass as an activator; when the content of CG in AAC was less than 30%, the compressive strength of the mixture was significantly greater than 40 Mpa. Zhu et al. [13] developed theoretical guidance and technical support for the concrete industry's large-scale and high-value use of coarse CG aggregates.

However, coal gangue fines (CGFs) generated through gangue aggregates have always been a concern. In typical gangue production, CGF accounts for about 20% of the total

amount of gangue [11,14]. There are few studies on the application of CGFs, a secondary waste generated during the resource utilization of CG. Consequently, the CGF becomes a secondary waste in addition to raw CG. The use of CGFs to avoid secondary contamination raises a new problem [15].

AAC consists of alkali activators and more than two precursors, and its main hydration product is C-S-H and C-(A)-S-H. Besides, there are N-A-S-H hydration products in alkali-activated metakaolin or fly ash cement. Herein, the binding capacity of AAC starts from the destruction of the bonds of Si-O-Si, Al-O-Si, Ca–O, and Al–O–Al in precursors under alkaline conditions. Both alkali-activated blast furnace slag cement and alkali-activated metakaolin or fly ash cement belong to AAC bonding systems [16,17].

Owing to the low activity of raw CG, different activation methods can improve the activity of CG. The activation methods of CG include mechanical activation [18], composite activation [4], chemical activation [19], microwave radiation activation [20], and thermal activation [21], of which thermal activation is the most common and essential. Thermal treatment can reduce the kaolinite crystallinity by destroying the layered structure and depolymerizing silica tetrahedrons of CGF. Under the action of high temperature, the kaolinite in the CG transforms into the metakaolin, and the calcination temperature is the direct source of the various activation effects [22]. Zhu et al. [15] discovered that kaolinite in CG was calcined at 800 °C; owing to the dehydroxylation of Al-(O, OH) octahedra and the depolymerization of Si-O tetrahedra, it was transformed into amorphous metakaolin with high pozzolanic activity.

Nowadays, CGF generated from the production of coal gangue aggregates receives less attention than coal gangue aggregate products. Most studies on using coal gangue as a supplementary cementitious material involve a grinding process other than the as-received secondary waste CGF. To fill this gap, this paper proposed to use calcined CGFs as the substitute replacement for slag in the preparation of AAC. Thermal activation (800 °C) was applied to enhance the reactivity of CGFs. This technology involves no grinding process and, more importantly, provides a more practical method to use CGF thanks to its low reactivity. In consideration of the above analysis, this paper proposed to use metakaolin as the replacement for ground granulated blast furnace slag in the preparation of AAC to explore the effect of metakaolin content (0%, 5%, 10%, 20%, 30%, and 40%) on the compressive strength and hydration products of AAC, and the strength decrease mechanism of AAC is analyzed in depth by microstructure.

2. Materials and Methods

2.1. Raw Materials

CG was collected from the Zhangji Mine in Huainan, China. It was crushed into coarse and fine aggregates for the preparation of concrete. Through that process, 200-mesh CGFs with sizes less than 75 μm were collected as secondary waste, used as recycled material in this research, and calcined in a muffle furnace (Nabertherm LT15/12, München, German) at 800 °C for two hours. Slag was provided by Shandong Kangcrystal New Materials Co. (Zibo, China). The Brunauer, Emmett, and Teller (BET) area was 1535 m^2/kg and the apparent density was 2800 kg/m^3. Table 1 shows the chemical compositions of metakaolin and slag.

Table 1. Chemical composition of raw materials.

Materials	Chemical Composition/% (XRF)							
	SiO_2	Al_2O_3	Fe_2O_3	CaO	MgO	K_2O	Na_2O	TiO_2
metakaolin	56.26	27.48	10.73	1.56	0.48	0.21	0.77	1.51
slag	27.37	15.47	0.30	44.95	7.58	0.33	0.35	0.73

The primary chemical components of metakaolin are SiO_2, Al_2O_3, and Fe_2O_3, as stated in Table 1. The main composition of slag is the aluminosilicate glass phase, composed of

SiO_2, Al_2O_3, and Fe_2O_3. The phase composition of metakaolin and slag was analyzed by XRD, as shown in Figure 1. Most metakaolin crystalline phases are quartz along with a small amount of illite and feldspar. The particle size distribution of CGF, slag, and sand is shown in Figure 2.

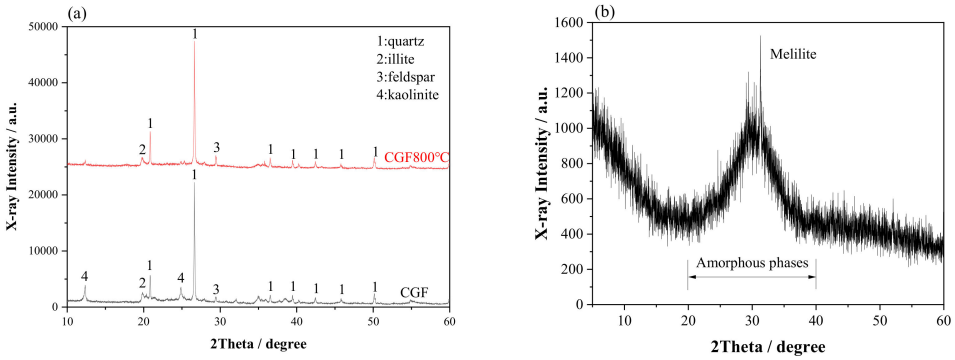

Figure 1. XRD pattern of raw materials: (**a**) CGF and (**b**) ground granulated blast furnace slag.

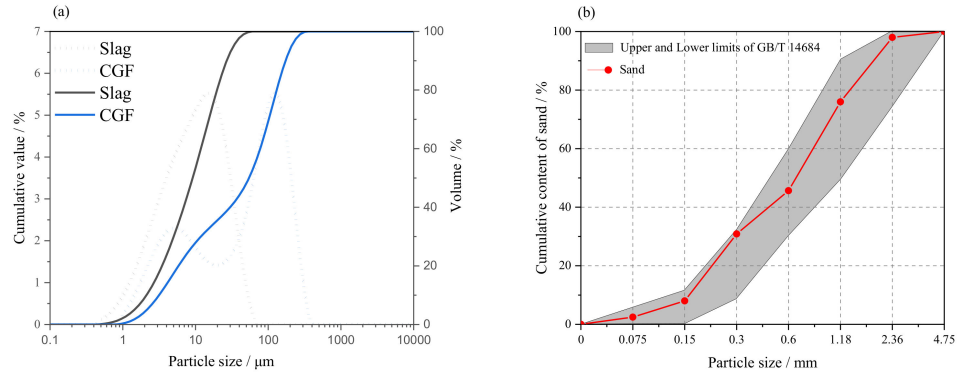

Figure 2. Particle size distribution of raw materials: (**a**) CGF with ground granulated blast furnace slag and (**b**) sand.

After calcination at 800 °C, the microstructure of CGF was destroyed, and kaolinite was dehydroxylated, the phase changed into metakaolin, and an uneven porous structure was formed [20]. The water used in the experiment was taken urban tap water. NaOH of analytical purity was purchased from Sinopharm Chemical Reagent Co., Ltd. (Shanghai, China). River sand with a finesse of 2.6 was used as the fine aggregates.

2.2. Mix Proportion and Sample Preparation

The granular metakaolin with a particle size smaller than 75 μm was calcined at 800 °C for 2 h. On the mix proportion of AAC, the precursors of the AAC were slag, as shown in Table 2, and CGFs treated with thermal procedures were used to replace the slag. The metakaolin-added AAC was thus named CGF5, CGF10, CGF20, CGF30, and CGF40, respectively. During the preparation of AAC, all dry materials were mixed in advance, and then water was added and mixed for 3 min.

Table 2. Experimental mix proportion (g/100 g).

	Sand	Slag	Water	NaOH	Metakaolin
Con	50	32.520	17.74	1.664	0
CGF5	50	30.894	17.74	1.664	1.626
CGF10	50	29.268	17.74	1.664	3.252
CGF20	50	26.016	17.74	1.664	6.504
CGF30	50	22.764	17.74	1.664	9.756
CGF40	50	19.512	17.74	1.664	13.008

2.3. Test Methods

2.3.1. Compressive Strength

The compressive strength of 50 mm × 50 mm × 50 mm cubic AAC specimens was measured at 3, 7, and 28 days. Three samples were tested for each mixing proportion, and the three test values were averaged to generate strength test values for each mixing ratio. The strength of specimens was measured under the testing conditions following ASTM C192.

2.3.2. X-ray Diffraction Tests

The chemical composition of samples was tested using X-ray diffraction (XRD). Proportional samples of all mixtures were analyzed timely after grinding the specimen to avoid carbonation. The diffraction pattern was obtained at (2θ) of 5°–60° with a scanning rate of 5°/min, and the step width was 0.02°. During the XRD test, each fine sample was scanned once. The XRD spectrum was analyzed by the commercial software Jade.

2.3.3. Scanning Electron Microscope Testing

A FlexSEM1000 scanning electron microscopy (SEM) was used to analyze the effect of metakaolin on the morphologic alteration of AAC paste. After the compressive strength test, representative samples were collected in ethanol to cease the hydration. The samples were coated with a gold layer for 2 min to achieve excellent electrical conductivity before testing. Then, the machine was started for observation.

2.3.4. Thermogravimetric Analysis Tests

TGA was utilized to investigate hydration products in cementitious material using a sample finely processed through a 200-mesh sieve. Without sand, samples were first produced in the proportions listed in Table 2. In the same curing chamber, it was cured for 28 days. Samples were collected, crushed, and immersed in ethanol for at least 24 h after the aging period to prevent hydration.

2.3.5. Fourier Transform Infrared Tests

The chemical linkages in the hydration products were studied using Fourier transform infrared spectroscopy (FTIR). The spectra had a wavenumber range of 500 to 4000 cm^{-1} and a resolution of 4 cm^{-1}. FT-IR measurements on the combination powder used the traditional KBr disc method.

3. Results and Discussions

3.1. Hydration Products Analyzed by TGA

Figure 3 shows the TGA spectra of six different amounts of metakaolin mixtures at various curing ages. Four endothermic peaks existed in the TGA-DTG curves. The first endothermic peak at around 60 °C could potentially be attributed to the decompositions of ettringite (Aft) [23]. Besides, the endothermic peaks at 140 °C and 380 °C are related to the dehydroxylation of C-(A)-S-H and dehydroxylation of the hydrotalcite-type phases [24,25]. Mass loss due to the decarbonization of calcite endothermic peak fell within ranges of 800 °C calcium carbonates [26]. Figure 3a shows the amount of burn loss for 3 d conserved in different groups under standard conditions. Figure 3b depicts the TGA and DTG results at the curing ages of 28 d. In contrast to Con, the exothermal peaks of metakaolin-added mixtures in the TGA-DTG curves are prominent. As AAC does not add carbonate in the mixing process, the formation of carbonate can be attributed to the carbonation of hydration products in the open-air curing process, and the higher the content of CGF, the more obvious the carbonation effect. Therefore, the mixture added with CGF is more likely to be carbonated. Compared with 3 d, C-(A)-S-H gel decreased, and ettringite (Aft) content increased after 28 days, which may be the reason for the increase in strength at 28 days.

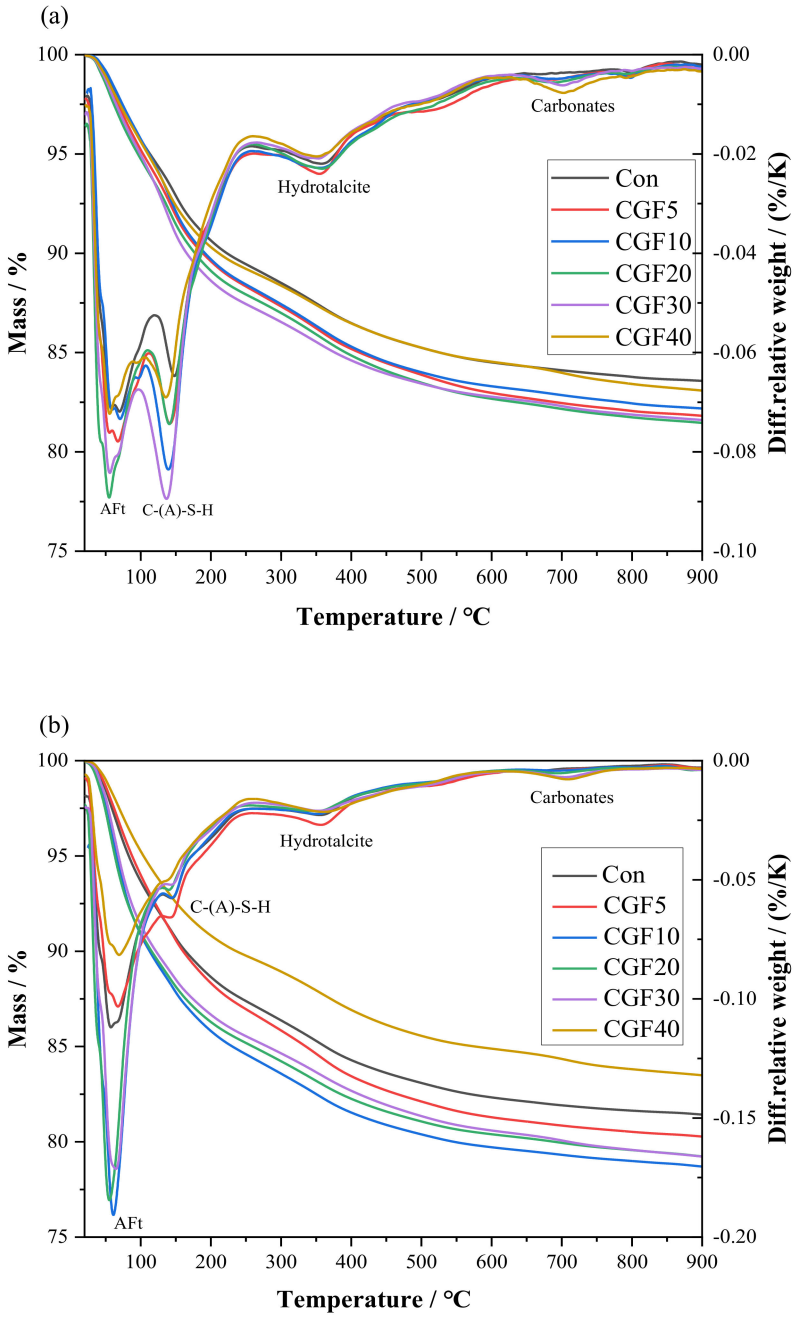

Figure 3. TGA-DTG curves of AAC: (**a**) 3 d and (**b**) 28 d.

3.2. XRD Analysis

XRD patterns of the AAC paste samples with 0, 5%, 10%, 20%, 30%, and 40% metakaolin at the age of 3 d and 28 d are shown in Figure 4. The diffraction peaks with 20 and 37° 2θ belong to C-(A)-S-H [27]. The C-(A)-S-H gel formed positively affects the compressive strength of alkali-activated metakaolin materials. As shown in Figure 4, the main crystalline phases of Figure 4 are identical, including hydrotalcite, C-A-S-H, quartz, and calcite. In contrast to Con, there is a quartz peak in the sample mixed with metakaolin, so adding metakaolin may change the product type of alkali-activated reaction. The peak value of crystal C-(A)-S-H diffraction peak increased at 28 d. The results show that the C-(A)-S-H gel structure tends to be more ordered. Because of calcium, carbonation occurs, the characteristic peak of calcite appears, and the formed C-(A)-S-H gel positively affects the compressive strength of alkali-activated metakaolin [28].

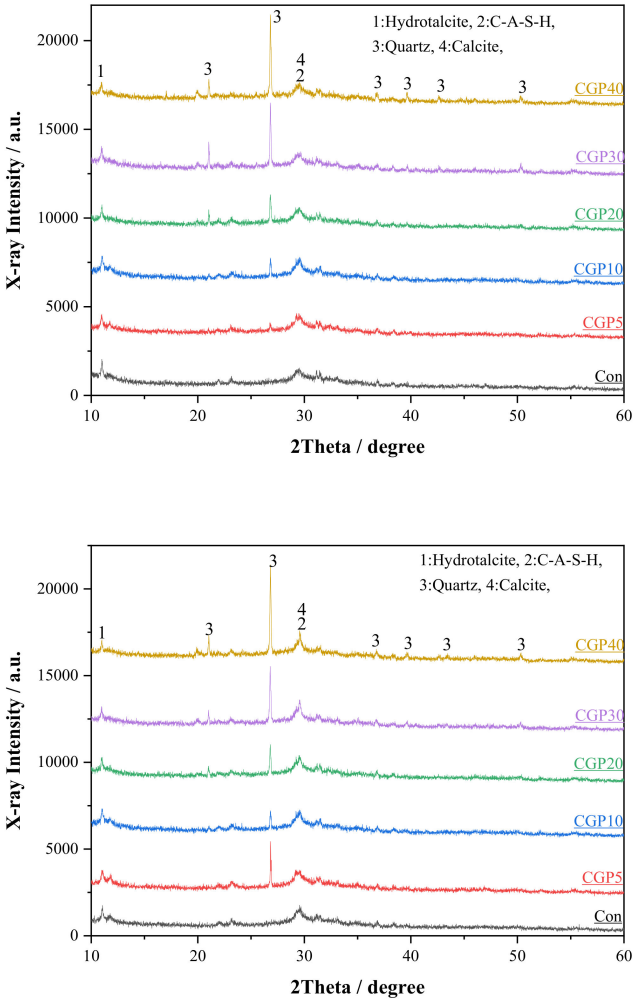

Figure 4. XRD spectra of AAC: 3 d and 28 d.

3.3. FTIR Analysis

Figure 5 shows the FTIR for the six groups in Table 2 at different ages of curing, and the spectral range was 500~4000 cm^{-1}. Figure 5a was conducted to observe the metakaolin and CGF from the view of molecule bonds, showing the FTIR spectra of CGF before and after being calcined at 800 °C in the range of 500–4000 cm^{-1}. The characteristic FTIR bands of AAC are usually distributed at around 1000 cm^{-1} and associated with the asymmetric stretching of Si-O-T (T = tetrahedral Si or Al) structures in hydration products [7,29]. The change in vibration peak reflects the bond characteristics of the hydration products and indicates, to some extent, the degree of polymerization of materials [30]. The absorption peak at 875 cm^{-1} corresponds to the asymmetric stretch of AlO_{4-} groups [31]. The bending vibration peak at about 3416 cm^{-1} refers to the H-OH bonds, which can be related to chemically combined water in the reaction products [32]. Each group absorption peak at 1410~1480 cm^{-1} was attributed to O-C-O stretching vibration. The AAC has produced few or no carbonates, which may result from carbonate being formed by the reaction of alkaline substances with carbon dioxide in the air, associated with that of XRD and TGA [33,34]. The characteristic band of the AAC gel product is located between the characteristic band of the N-A-S-H gel (1030 cm^{-1}) and the characteristic band of the C-(A)-S-H gel (940 cm^{-1}); therefore, it is not a single gel product in AAC [35]. For samples cured at 3 d and 28 d, the Si-O-T (T = tetrahedral Si or Al) band shifts from 995 cm^{-1} to 947 cm^{-1}, associated with the variation of hydration products. This observation suggests the further development of gel products with prolonged curing in all samples, which is in good agreement with the change in the fraction of gel products estimated by TGA testing [36].

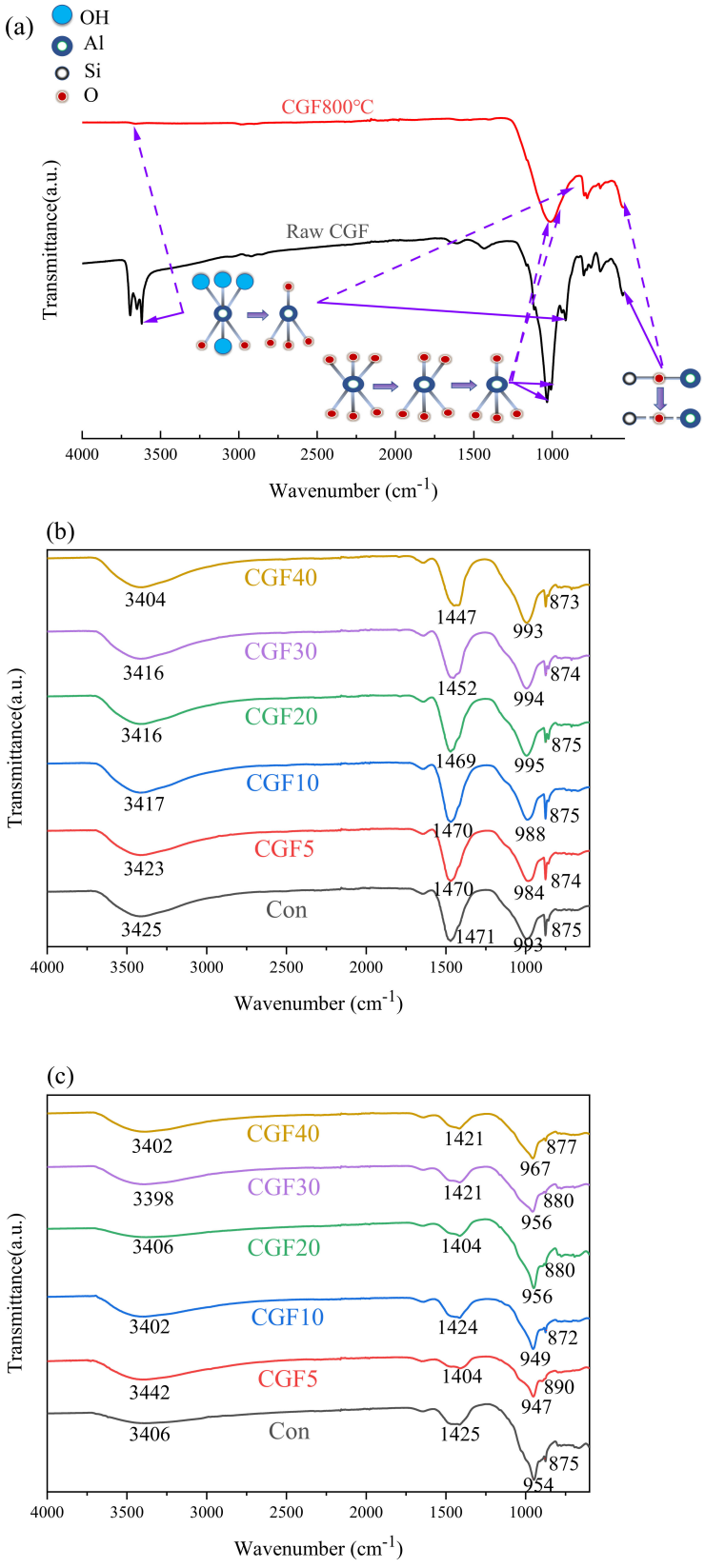

Figure 5. FT-IR spectrum of AAC: (**a**) comparison results of FTIR patterns of metakaolin; (**b**) 3 d; and (**c**) 28 d.

3.4. Compressive Strength

Figure 6 shows the compressive strength of AAC under different content metakaolin (0%, 5%, 10%, 20%, 30%, and 40%) at 3 d, 7 d, and 28 d. The compressive strength of all specimens increases with time and has nothing to do with the content of metakaolin. As shown in Figure 6, The compressive strength is enhanced with increased CGF content from 0% to 10%. However, compressive strength decreases as the CGF content increases from 10% to 40%. More specially, the addition of 10% metakaolin showed optimal increments in the compressive strength of AAC, and the values were 8%, 25%, and 13% at 3 d, 7 d, and 28 d, respectively. When the content of metakaolin reaches 20%, 30%, and 40%, the 28 d compressive strength of the designed mixes sample decreases by 13%, 24%, and 44%, respectively, indicating that the higher addition of metakaolin has a negative on the compressive strength. The development of the compressive strength of the AAC is attributed to the production of silicoaluminate polymer. With the addition of metakaolin, the hydration product combines C-(A)-S-H gel and N-A-S-H gel.

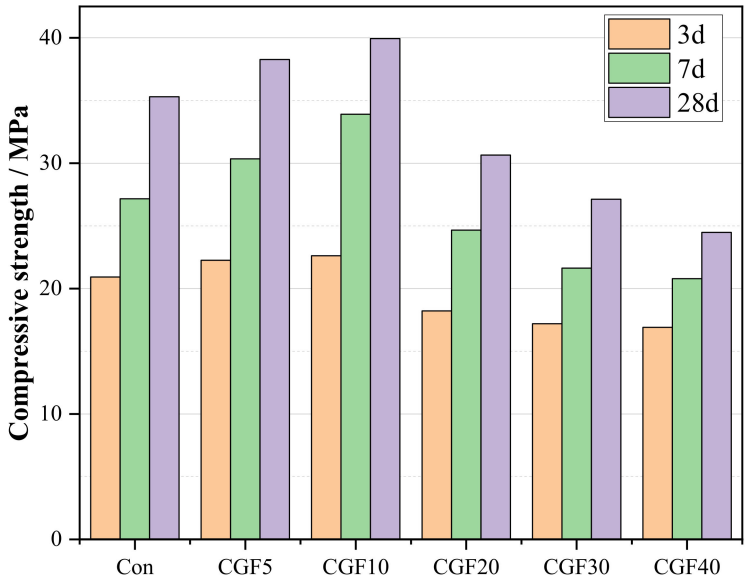

Figure 6. Compressive strength development of AAC.

However, with the increased metakaolin, the increased active SiO_2 content decreases the Ca/Si ratio. Furthermore, many metakaolin particles in the AAC are unreacted in the mixtures. Thus, the pores are filled with these unreacted CGF particles, resulting in decreased strength owing to insufficient polymerization [6].

3.5. Microstructure Analyzed by SEM

Figure 7 shows the scanning electron microscopy (SEM) photos of metakaolin and ground granulated blast furnace slag. It can be seen that the uncalcined CGF has a "scale-shaped" lamellar stable crystallographic structure. However, the metakaolin formed after calcination has a higher pozzolanic effect, which can better react with cementitious materials to achieve higher strength. Figure 8 presents typical SEM images of AAC with metakaolin with different contents. It can be seen that there are gelatin-like, flocculent products and some spongy calcium–aluminum hydrate particles on the surface of each group of samples, forming a relatively dense microstructure; as can be found in Figure 8a, needle-like products formed on the surface of surrounding pastes and cracks caused by self-shrinkage in the curing ages [37]. Figure 8b–f are the SEM images of AAC with metakaolin. With metakaolin as the cementitious material, the resulting hydration products of AAC are C-A-S-H gels, C-S-H gels, and N-A-S-H gels. The three gels are intertwined to form a reticular disorder structure of AAC. However, replacing slag with a large amount of metakaolin will decrease

the Ca/Si ratio, increase N-A-S-H gels, and decrease C-(A)-S-H gels, which is a fundamental reason for the decrease in compressive strength in the curing ages [38]. Furthermore, the massive unreacted metakaolin on the surface in Figure 8f loosens the AAC structure, increases the porosity, and reduces the intensity of polymerization [39].

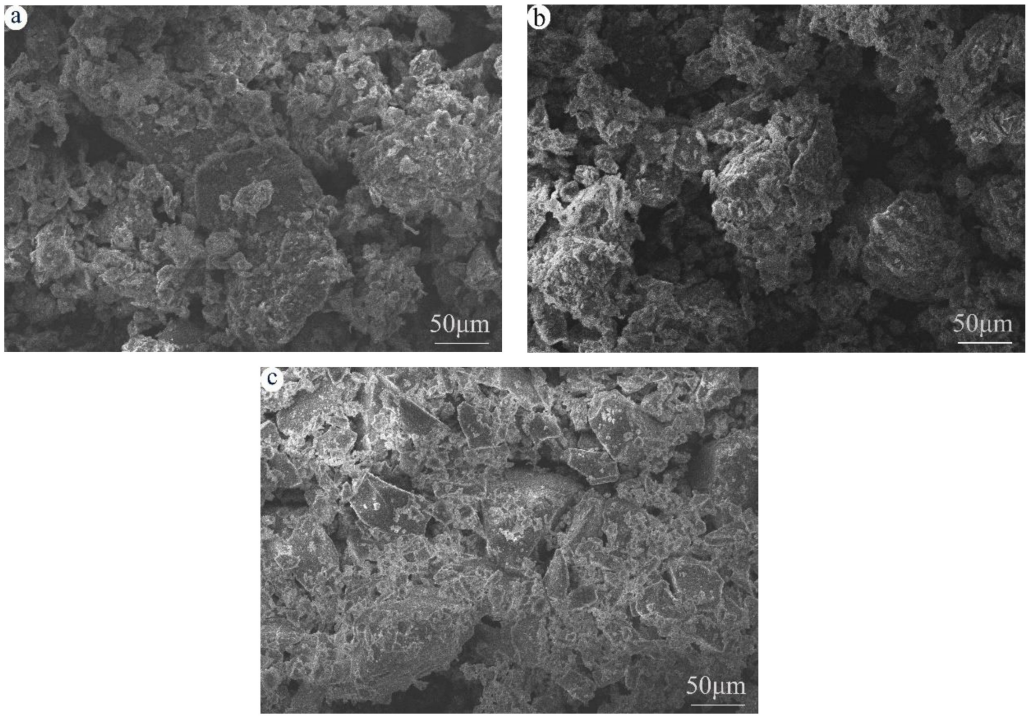

Figure 7. SEM images of (**a**) raw CGF; (**b**) metakaolin; and (**c**) ground granulated blast furnace slag.

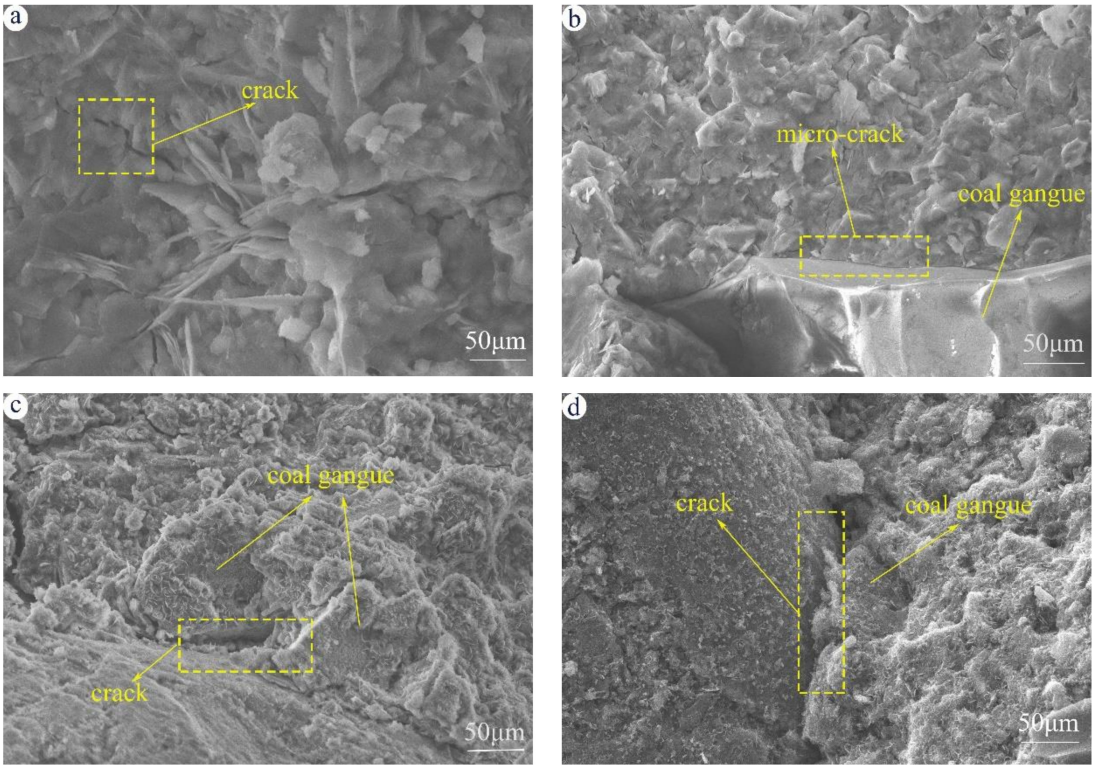

Figure 8. *Cont.*

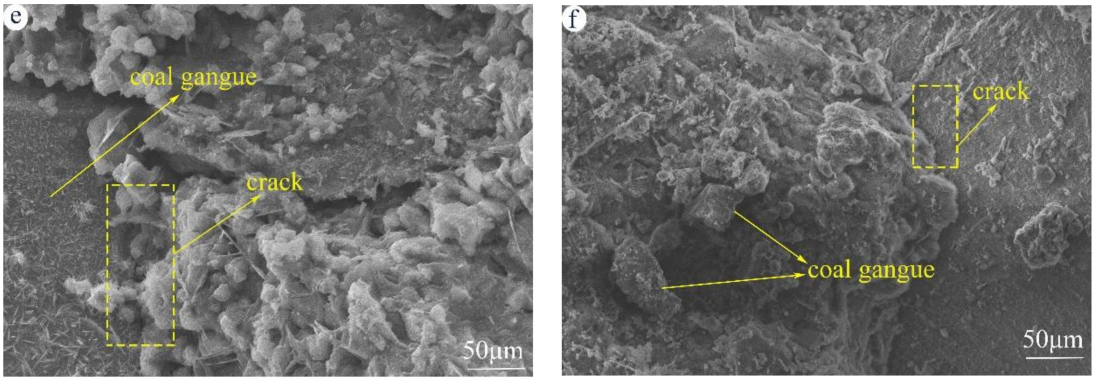

Figure 8. SEM images of AAC with and without metakaolin: (**a**) Con; (**b**) CGF5; (**c**) CGF10; (**d**) CGF20; (**e**) CGF30; and (**f**) CGF40.

4. Conclusions

The mechanical strength development of AAC slag replaced by metakaolin with different dosages was studied, and the hydration products and microstructure of AAC were tested. The results show that different contents of metakaolin samples have different effects on AAC.

(1) The experimental results confirmed that the metakaolin could be used to substitute slag. CGF10 presents higher mechanical strength compared with Con. The highest compressive strength is achieved at 39.9 MPa after 28 days of curing when metakaolin replaces 10% slag.
(2) High-content metakaolin samples present lower mechanical strength, slower setting, and minor heat release than samples formulated with a lower metakaolin.
(3) The type of gel products formed in AAC does not vary significantly with the content of CGF. However, the increase in the content of metakaolin increases the C-(A)-S-H in gel products.
(4) The internal structure and chemical properties of CGF changed significantly after calcination. In the calcination process, CGF underwent a dehydroxylation reaction, resulting in an increase in its activity. The effect of aggregate filling in the early stage of CGF and the pozzolanic effects can enhances the strength of AAC.

Author Contributions: C.L.: Investigation, Writing—Original Draft Preparation. C.W.: Conceptualization, Writing—Reviewing and Editing, and Supervision. J.W.: Investigation. M.G.: Investigation. All authors have read and agreed to the published version of the manuscript.

Funding: This work was supported by the Graduate Innovation Fund Project of Anhui University of Science and Technology (2021CX2039).

Institutional Review Board Statement: Not applicable.

Informed Consent Statement: Informed consent was obtained from all subjects involved in the study.

Data Availability Statement: Not applicable.

Conflicts of Interest: The authors declare that they have no known competing financial interests or personal relationships that could have appeared to influence the work reported in this document.

References

1. Huang, G.; Ji, Y.; Li, J.; Hou, Z.; Dong, Z. Improving strength of calcinated coal gangue geopolymer mortars via increasing calcium content. *Constr. Build. Mater.* **2018**, *166*, 760–768. [CrossRef]
2. Wang, X.; Zhu, K.; Zhang, L.; Li, A.; Ullah, F.; Chen, C.; Huang, J.; Zhang, Y. Preparation of high-quality glass-ceramics entirely derived from fly ash of municipal solid waste incineration and coal enhanced with pressure pretreatment. *J. Clean. Prod.* **2021**, *324*, 129021. [CrossRef]

3. Lasek, J.A.; Głód, K.; Słowik, K. The co-combustion of torrefied municipal solid waste and coal in bubbling fluidised bed combustor under atmospheric and elevated pressure. *Renew. Energy* **2021**, *179*, 828–841. [CrossRef]
4. Zhao, Y.; Yang, C.; Li, K.; Qu, F.; Yan, C.; Wu, Z. Toward understanding the activation and hydration mechanisms of composite activated coal gangue geopolymer. *Constr. Build. Mater.* **2022**, *318*, 125999. [CrossRef]
5. Hongqiang, M.A.; Cheng, Y.I.; Chen, H.; Shi, J.; Weijian, L.I.; Guo, Y. Property and Cementation Mechanism of Alkali-activated Coal Gangue-slag Cementitious Materials. *Chin. J. Mater. Res.* **2018**, *32*, 898–904. [CrossRef]
6. Ma, H.; Zhu, H.; Wu, C.; Chen, H.; Sun, J.; Liu, J. Study on compressive strength and durability of alkali-activated coal gangue-slag concrete and its mechanism. *Powder Technol.* **2020**, *368*, 112–124. [CrossRef]
7. Guo, L.; Zhou, M.; Wang, X.; Li, C.; Jia, H. Preparation of coal gangue-slag-fly ash geopolymer grouting materials. *Constr. Build. Mater.* **2022**, *328*, 126997. [CrossRef]
8. Wang, A.; Hao, F.; Liu, P.; Mo, L.; Liu, K.; Li, Y.; Cao, J.; Sun, D. Separation of calcined coal gangue and its influence on the performance of cement-based materials. *J. Build. Eng.* **2022**, *51*, 104293. [CrossRef]
9. Salguero, F.; Grande, J.A.; Valente, T.; Garrido, R.; de la Torre, M.L.; Fortes, J.C.; Sánchez, A. Recycling of manganese gangue materials from waste-dumps in the Iberian Pyrite Belt—Application as filler for concrete production. *Constr. Build. Mater.* **2014**, *54*, 363–368. [CrossRef]
10. Li, Y.; Liu, S.; Guan, X. Multitechnique investigation of concrete with coal gangue. *Constr. Build. Mater.* **2021**, *301*, 124114. [CrossRef]
11. Zhou, M.; Dou, Y.; Zhang, Y.; Zhang, Y.; Zhang, B. Effects of the variety and content of coal gangue coarse aggregate on the mechanical properties of concrete. *Constr. Build. Mater.* **2019**, *220*, 386–395. [CrossRef]
12. Han, J.Y.; Song, X.Y.; Gao, Z.H. Excitation Effect of Soluble Glass on Composite System with Calcined Coal Gangue and Slag. *Appl. Mech. Mater.* **2012**, *174*, 30–34. [CrossRef]
13. Zhu, Y.; Zhu, Y.; Wang, A.; Sun, D.; Liu, K.; Liu, P.; Chu, Y. Valorization of calcined coal gangue as coarse aggregate in concrete. *Cem. Concr. Compos.* **2021**, *121*, 104057. [CrossRef]
14. Dong, Z.; Xia, J.; Fan, C.; Cao, J. Activity of calcined coal gangue fine aggregate and its effect on the mechanical behavior of cement mortar. *Constr. Build. Mater.* **2015**, *100*, 63–69. [CrossRef]
15. Wu, C.; Jiang, W.; Zhang, C.; Li, J.; Wu, S.; Wang, X.; Xu, Y.; Wang, W.; Feng, M. Preparation of solid-waste-based pervious concrete for pavement: A two-stage utilization approach of coal gangue. *Constr. Build. Mater.* **2022**, *319*, 125962. [CrossRef]
16. Rahman, R.; Rakhimov, R.Z.; Rakhimova, N.R.; Ojovan, I. *Cementitious Materials for Nuclear Waste Immobilization*; John Wiley & Sons: Hoboken, NJ, USA, 2014.
17. Shi, C.; Fernández-Jiménez, A. Stabilization/solidification of hazardous and radioactive wastes with alkali-activated cements. *J. Hazard. Mater.* **2006**, *137*, 1656–1663. [CrossRef]
18. Geng, J.; Zhou, M.; Li, Y.; Chen, Y.; Han, Y.; Wan, S.; Zhou, X.; Hou, H. Comparison of red mud and coal gangue blended geopolymers synthesized through thermal activation and mechanical grinding preactivation. *Constr. Build. Mater.* **2017**, *153*, 185–192. [CrossRef]
19. Li, Y.; Yao, Y.; Liu, X.; Sun, H.; Ni, W. Improvement on pozzolanic reactivity of coal gangue by integrated thermal and chemical activation. *Fuel* **2013**, *109*, 527–533. [CrossRef]
20. Guan, X.; Chen, J.; Zhu, M.; Gao, J. Performance of microwave-activated coal gangue powder as auxiliary cementitious material. *J. Mater. Res. Technol.* **2021**, *14*, 2799–2811. [CrossRef]
21. Hao, R.; Li, X.; Xu, P.; Liu, Q. Thermal activation and structural transformation mechanism of kaolinitic coal gangue from Jungar coalfield, Inner Mongolia. *China Appl. Clay Sci.* **2022**, *223*, 106508. [CrossRef]
22. Cao, Z.; Cao, Y.; Dong, H.; Zhang, J.; Sun, C. Effect of calcination condition on the microstructure and pozzolanic activity of calcined coal gangue. *Int. J. Miner. Process.* **2016**, *146*, 23–28. [CrossRef]
23. Yuan, B.; Yu, Q.L.; Brouwers, H.J.H. Evaluation of slag characteristics on the reaction kinetics and mechanical properties of Na_2CO_3 activated slag. *Constr. Build. Mater.* **2017**, *131*, 334–346. [CrossRef]
24. Chen, W.; Li, B.; Wang, J.; Thom, N. Effects of alkali dosage and silicate modulus on autogenous shrinkage of alkali-activated slag cement paste. *Cem. Concr. Res.* **2021**, *141*, 106322. [CrossRef]
25. Chen, Z.; Ye, H. Influence of metakaolin and limestone on chloride binding of slag activated by mixed magnesium oxide and sodium hydroxide. *Cem. Concr. Compos.* **2022**, *127*, 104397. [CrossRef]
26. Zhang, L.; Chen, P.; Xu, Y.; Hu, X.; Wang, Y. Upcycling waste flavedo into a bio-admixture of set retarder and compressive strength enhancer for cement-based materials. *J. Clean. Prod.* **2022**, *332*, 130060. [CrossRef]
27. Li, Z.; Gao, Y.; Zhang, J.; Zhang, C.; Chen, J.; Liu, C. Effect of particle size and thermal activation on the coal gangue based geopolymer. *Mater. Chem. Phys.* **2021**, *267*, 124657. [CrossRef]
28. Bernal, S.A.; Provis, J.L.; Rose, V.; Mejía de Gutierrez, R. Evolution of binder structure in sodium silicate-activated slag-metakaolin blends. *Cem. Concr. Compos.* **2011**, *33*, 46–54. [CrossRef]
29. Farmer, V.C. *The Infrared Spectra of Minerals*; Mineralogical Society: London, UK, 1974; Volume 4.
30. Uchino, T.; Sakka, T.; Iwasaki, M. Interpretation of Hydrated States of Sodium Silicate Glasses by Infrared and Raman Analysis. *J. Am. Ceram. Soc.* **2010**, *74*, 306–313. [CrossRef]
31. Gadsden, J.A. *Infrared Spectra of Minerals and Related Inorganic Compounds*; Butterworths: London, UK, 1975.

32. Bernal, S.A.; de Gutierrez, R.M.; Provis, J.L.; Rose, V. Effect of silicate modulus and metakaolin incorporation on the carbonation of alkali silicate-activated slags. *Cem. Concr. Res.* **2010**, *40*, 898–907. [CrossRef]
33. Li, N.; Farzadnia, N.; Shi, C. Microstructural changes in alkali-activated slag mortars induced by accelerated carbonation. *Cem. Concr. Res.* **2017**, *100*, 214–226. [CrossRef]
34. Ye, T.; Min, X.; Li, X.; Zhang, S.; Gao, Y. Improved holding and releasing capacities of coal gangue toward phosphate through alkali-activation. *Chemosphere* **2022**, *287*, 132382. [CrossRef] [PubMed]
35. Zhang, Z.; Provis, J.L.; Wang, H.; Bullen, F.; Reid, A. Quantitative kinetic and structural analysis of geopolymers. Part 2. Thermodynamics of sodium silicate activation of metakaolin. *Thermochim. Acta* **2013**, *565*, 163–171. [CrossRef]
36. Zhang, M.; Zhao, M.; Zhang, G.; El-Korchi, T.; Tao, M. A multiscale investigation of reaction kinetics, phase formation, and mechanical properties of metakaolin geopolymers. *Cem. Concr. Compos.* **2017**, *78*, 21–32. [CrossRef]
37. Melo Neto, A.A.; Cincotto, M.A.; Repette, W. Drying and autogenous shrinkage of pastes and mortars with activated slag cement. *Cem. Concr. Res.* **2008**, *38*, 565–574. [CrossRef]
38. Garcia-Lodeiro, I.; Palomo, A.; Fernández-Jiménez, A.; Macphee, D.E. Compatibility studies between N-A-S-H and C-A-S-H gels. Study in the ternary diagram Na_2O–CaO–Al_2O_3–SiO_2–H_2O. *Cem. Concr. Res.* **2011**, *41*, 923–931. [CrossRef]
39. Cheng, Y.; Hongqiang, M.; Hongyu, C.; Jiaxin, W.; Jing, S.; Zonghui, L.; Mingkai, Y. Preparation and characterization of coal gangue geopolymers. *Constr. Build. Mater.* **2018**, *187*, 318–326. [CrossRef]